

PCCP

Accepted Manuscript



This is an *Accepted Manuscript*, which has been through the Royal Society of Chemistry peer review process and has been accepted for publication.

Accepted Manuscripts are published online shortly after acceptance, before technical editing, formatting and proof reading. Using this free service, authors can make their results available to the community, in citable form, before we publish the edited article. We will replace this *Accepted Manuscript* with the edited and formatted *Advance Article* as soon as it is available.

You can find more information about *Accepted Manuscripts* in the [Information for Authors](#).

Please note that technical editing may introduce minor changes to the text and/or graphics, which may alter content. The journal's standard [Terms & Conditions](#) and the [Ethical guidelines](#) still apply. In no event shall the Royal Society of Chemistry be held responsible for any errors or omissions in this *Accepted Manuscript* or any consequences arising from the use of any information it contains.



Journal Name

ARTICLE

Multi-slices nanostructured WS₂@rGO with enhanced Li-batteries performance and a comprehensive investigation of mechanism

Honglin Li, Ke Yu*, Hao Fu, Bangjun Guo, Xiang Lei and Ziqiang Zhu

Received 00th January 20xx,
Accepted 00th January 20xx

DOI: 10.1039/x0xx00000x

www.rsc.org/

The thin nanoslice structured WS₂@reduced graphene oxide (rGO) composite was successfully fabricated by a facile hydrothermal synthesis method. The layered structure and morphology of the composite were investigated by X-ray diffraction (XRD), field emission scanning electron microscopy (FESEM) and transmission electron microscopy (TEM). The WS₂@rGO composite structure demonstrated significantly enhanced rate capability performance in comparison with pristine WS₂ when used as anode material for lithium-ion batteries (LIBs). The specific capacity of the composite showed a capacity of 565 mAh/g after 100 cycles when cycled at 0.1 A/g and it could still deliver a stable capacity of about 337 mAh/g at 2 A/g. Electrochemical impedance spectroscopy (EIS) measurement showed that the synergy effect between WS₂ and rGO could remarkably reduce the contact resistance and improve the corresponding electrochemical performances. In order to analyze and interpret the corresponding results from a theoretical sound perspective, the first principles calculation was further performed to investigate the corresponding inner mechanism of pristine WS₂ and WS₂@graphene composite. Nudged elastic band (NEB) method was used to investigate the diffusion properties of Li in different structures. Molecular dynamics (MD) simulation and Young's modulus calculation were further employed to explore the stability and mechanical properties of the two structures for the first time. These new perspectives pave the way for the design and fabrication of graphene-TMDs based composites as the next generation LIBs anode materials with high power density and cycle stability.

1 Introduction

In order to alleviate the continuously increased environmental crisis from greenhouse gas pollution of modern transportation, the developing of high power LIBs is becoming increasingly urgent for the utilization and storage of sustainable energy. It has been extensively reported that excellent electrochemical performances can be obtained from the nanostructured electrode materials for the advantages of enhanced contact area, the improved conductivity and the promoted stability.¹⁻³ At present, the most widely used anode material in commercialized LIBs is graphite, while it only delivers a poor capacity of 372 mAh/g in theory. Therefore, researchers have been committed to exploring new anode materials with a higher reversible specific capacity and a longer cycle life simultaneously for LIBs usage.⁴ Ever since the discoveries and applications of graphene-like nanomaterials (MoS₂, WS₂, BN, V₂O₅, etc.), two-dimensional (2D) layered structures have been a hot area for several years in industrial and scientific fields for their special properties, such as narrow band gap, diverse structures and morphologies, which have attracted considerable attentions for they are promising

substitutes for anode materials of LIBs.⁵⁻⁷ WS₂ has a high theoretical specific capacity (433 mAh/g based on 4 mol of Li⁺ insertion) compare to that of the commercial graphite. This is because the stacked WS₂ layers with weak van der Waals interaction can ensure an easy intercalation/de-intercalation reactions of Li⁺ and store massive Li ions. Besides, the interlayer spacing of WS₂ (0.616 nm) is significantly larger than that of graphite (0.335 nm), suggesting the intercalation/de-intercalation processes of lithium ions for layered WS₂ should be easier compared with graphite and thus the geometrical configuration of the active substances can be maintained without an apparent expansion or degeneration in the corresponding electrochemical processes, making it a potential alternative of graphite.⁸

Recently, a variety of WS₂ nanostructures with diverse morphologies and constructions have been fabricated for LIBs usage, while the storage capacity and cycle stability still leave much to be desired and some defects hinder their further development. Firstly, the intermediate product Li₂S in the corresponding conversion processes is liable to react with the electrolyte and the formation of a thick gel-like polymeric layer will inhibit the following reactions and result in the degraded capacity and stability,⁹ which has been reported in other metal sulfide based electrode materials.^{10, 11} Besides, the poor electrical conductivity can lead to the destruction of geometric architecture during cyclic processes following by a rapid performance degradation. The above are the major problems

Key Laboratory of Polar Materials and Devices (Ministry of Education of China),
Department of Electronic Engineering, East China Normal University, Shanghai
200241, China

*Corresponding author. E-mail address: yk5188@263.net

faced by the extensive use of WS_2 based LIBs. Out of the above considerations, combining WS_2 with a conductive matrix for a faster electron transfer during the charge/discharge processes should be an effective way to perfect the corresponding electrochemical performances.¹² Aside from the conductive polymers,¹³ carbon materials have also been widely used to composite WS_2 to enhance the overall performance.¹⁴ Graphene has excellent electrochemical characteristic and mechanical strength, it is supposed to be an ideal compound material.¹⁵ The compatibility of 2D structured graphene and WS_2 makes them can composite together and achieve the ideal performance.¹⁶ On the one hand, the excellent electrical conductivity of graphene facilitates the corresponding electrochemical processes in electrode reactions, for another, it can also cushion the structure degradation in the intercalation/de-intercalation reactions of Li ions for its outstanding mechanical properties.¹⁷ Therefore, this composition form can significantly improve the overall performance by taking full advantages of the two portions. It is expected that the composite will exhibit increased capacity and enhanced cycling stability in comparison with pristine WS_2 . It will provide large electrode/electrolyte contact area during the electrochemical reactions, promote the transfer of electrons as well as maintain the stability of active material during lithiation and de-lithiation processes. In experiments, Liu *et al.* synthesized WS_2 and GO nanosheets lamellar composite films by filtration. After hydrothermal reduction, the flexible lamellar WS_2 @rGO paper was evaluated as binder-free anodes for LIBs, which presented a reversible capacity 8 times higher than that of pristine WS_2 nanosheets. They attributed the improved performances to the uniformly alternated lamellar structures, efficiently inhibited WS_2 sheets' restacking, increased conductivity of the electrode and the suppressed volume expansion during Li^+ intercalation/de-intercalation processes.¹⁸ Xu *et al.* fabricated few layered WS_2 @graphene nanosheets through a facile hydrothermal method and a following freeze-drying treatment. The two-step approach synthesized WS_2 @graphene composite presented excellent cycling stability and superior rate capability.¹⁹ Liu *et al.* fabricated WS_2 @rGO hybrid paper cross-linked by PEO via a simple and scalable method. The synthesized composite exhibited high capacity, good cycle stability and rate performance for lithium storage.²⁰

In this work, we report the fabrication of multi-slices nanostructured WS_2 @rGO through a facile hydrothermal process for reversible Li^+ storage. The composite exhibited excellent cycling stability and outstanding high-rate capability of lithium storage. Besides, to our knowledge, there is still no report on the theoretical study of WS_2 @graphene composite in LIBs usage. In order to elucidate the internal mechanisms for the improved LIBs performances, we constructed the Li_2S inserted model based on experiment data and analysed the binding energies, charge density difference, diffusion properties and stabilities of the two structures by the first-principles calculation detailedly. In short, the computed results fully explain the reason why WS_2 @rGO composite structure exhibits better performances and the corresponding analytical

methods also can be extended for future studies of the other layered 2D materials based LIBs with high performances.

2 Experimental

2.1 Synthesis of WS_2 @rGO (WG)

The reduction of GO to rGO is a widely used method to fabricate graphene based materials. In this work, the graphene oxide (GO) nanosheets were exfoliated from natural graphite by the modified Hummer's method as reported previously.²¹ The WS_2 @rGO composite was synthesized by a one-step hydrothermal method. 80 mg GO, 5 mmol $Na_2WO_4 \cdot 2H_2O$, 0.02 mol NH_2CSNH_2 and 0.01 mol of $NH_2OH \cdot HCl$ were dissolved into 60 mL deionized water and the mixed liquor was magnetic stirred for 30 min. Then, the mixture solution was transferred to a 100 mL Teflon lined stainless-steel autoclave and heated at 200 °C for 24 h. After naturally cooled down to room temperature, the composite was obtained and washed by distilled water and anhydrous ethanol alternately, then dried at 60 °C for 12 h. The synthesis procedures of pristine WS_2 were the same with the above composite without GO being added.

2.2 Characterization of WG Nanostructures

A FESEM (JEOL-JSM-6700F, operating accelerating voltage of 20 kV) was used to analyze the morphology and structure of the synthesized nanostructures, XRD measurements were conducted using Cu $K\alpha$ radiation ($\lambda = 1.5418 \text{ \AA}$) (Bruker D8 Advance diffract meter) and TEM (JEOL-JEM-2100) at an accelerating voltage of 200 kV. X-ray photoelectron spectrometry (XPS) measurements were conducted with an ESCALAB 250Xi instrument using monochromatic Al $K\alpha$ radiation. Raman spectra analyses were carried out on a Jobin-Yvon Lab RAM HR 800 micro-Raman spectrometer. All the above measurements were performed at room temperature.

2.3 Electrochemical Measurements

The electrochemical performances of pristine WS_2 and WG composite were evaluated through two-electrode coin-type cells (CR 2025) under room temperature. The active material, carbon black and PVDF were prepared in a weight ratio of 8: 1: 1 on a copper foil as the working electrodes. The obtained slurry was spread on a copper foil with a thickness of 0.02 mm. Then, the coated copper foils were treated in a vacuum at 100 °C for 12 h and then pressed to form a working electrode with a typical active material loading of 1.5 mg cm^{-2} . All cells related procedures were performed in an Ar-filled glove box. Li foils were served as the counter electrode and Celgard 2400 polypropylene films were acted as the separator. The electrolyte was 1 M $LiPF_6$ in ethylene carbonate/ diethyl carbonate. The charge and discharge cycles of the cells were carried out on a LAND-CT2001A battery measurement system under various voltage range between 0.01 V and 3.0 V. The cyclic voltammetry (CV) were obtained on a CH Instrument 660C at a scan rate of 0.5 mV s^{-1} . EIS surveys were conducted ranging from 100 KHz to 0.01 KHz.

2.4 Computational Details

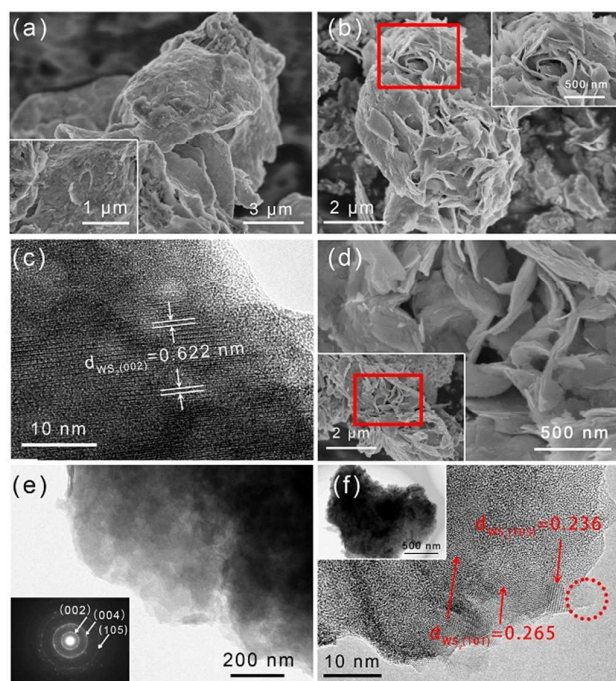


Fig. 1 SEM and TEM images of the pristine WS_2 and WG composite. (a) The SEM images of the pristine WS_2 in low- and medium-magnifications. (b) and (d) are SEM images of the WG composite in different magnifications. (c) HRTEM images of the pristine WS_2 . (e) and (f) are the TEM and HRTEM images of WG composite. Inset figure in (e) is the selected area electron diffraction (SAED) pattern of WG.

In this section, we performed the comprehensive first-principles calculation to study the detailed properties of the different structures. All calculation were performed using DFT, as implemented in the Vienna ab initio Simulation Package (VASP).²² The generalized gradient approximation (GGA) functional of Perdew, Burke and Ernzerhof (PBE) was used to deal with the exchange and correlation potentials.²³ The spacing of 15 Å was used to avoid interlayer interactions. A $5 \times 5 \times 1$ Monkhorst-Pack k-point sampling for the Brillouin zone k-point mesh and a 450 eV cutoff energy were used for the calculation. All initiating structures have been fully relaxed until the convergence criteria of energy and force were less than 10^{-5} eV and $0.01 \text{ eV } \text{Å}^{-1}$, respectively. The evolution of the system was derived using the molecular dynamics (MD) method at a time-step of 3.0 ps for $\text{W}_{32}\text{S}_{64}\text{Li}_2$ and $\text{W}_{16}\text{S}_{32}\text{C}_{45}\text{Li}_2$ structures. Starting from the initial configuration, the positions of all the atoms were relaxed at given temperatures of 600, 900 and 1200 k with 1000 MD steps. 3 ps is sufficient to evaluate the WS_2 and WS_2 @Graphene systems. The Young's modulus were determined by finite distortions of the lattice and the corresponding values were obtained from the strain–stress relationship.

3. Results and Discussion

3.1 Characterization of the Synthesized Samples

Fig. 1a is the SEM image of pristine WS_2 , it shows bulk morphology and the surface of the synthesized product is smooth and has no specific 3D configuration. Fig. 1c shows the

corresponding HRTEM image of the pristine WS_2 , which proves the aggregated nature of pristine WS_2 . The pristine WS_2 is composed of multilayered structure and the interlayer distance between WS_2 layers is estimated to be 0.622 nm, which corresponds to the d-spacing value of the (002) plane. Fig. 1b and d show SEM images of the WG composite. It is distinctly different from the pristine WS_2 . The surface of the synthesized WG composite exhibits massive laminated structures that obviously differ from the pristine WS_2 , implying this multilayered organization can provide much more active sites to be utilized in the corresponding electrochemical processes and make more efficient use of WS_2 . The nanoslices demonstrated in inset Fig. 1b and d indicate that WS_2 in WG composite are grown in a free and loose way and can provide a large electrode/electrolyte contact area during the electrochemical reactions. The layered WS_2 in the composite structure are mainly consisted of the WS_2 with limited-layer and tightly combined with rGO sheets. The following TEM image of the WG composite shown in Fig. 1e reveals a scattered and mild construction of WS_2 grown on rGO sheets characterized by various shades. The low magnification TEM image (Fig. 1e) presents a typical piece of a WG nanoslice. Its SAED pattern displays rings feature, which can be well indexed to (002), (004) and (105) crystal planes of the hexagonal WS_2 , indicating the crystalline characteristic of the synthesized WG composite. From the lattice resolved HRTEM image shown in Fig. 1f, the interlayer gap of the (103) and (101) crystal planes can be directly observed and the red circle shows the base of rGO. Generally, the formation of WG nanocomposite has relation with the nucleation in certain reaction conditions of amorphous primary nanoparticles. Numerous amorphous WS_2 structures take shape in the solution during the primary reaction period, where the added NH_2CSNH_2 acts as S resource and reductant simultaneously. These primary structures can spontaneously and freely aggregate into spheres and then curl to structured petals gradually at the surface for the layered nature of WS_2 when the temperature and pressure exceed certain levels. The initial GO sheets can be easily reduced to rGO by H_2S released from NH_2CSNH_2 . It is considered that the formation of WG composite is greatly influenced by the oxygenated functional groups in GO. WS_2 may grow in these active sites in the process of the GO hydrothermal reducing to rGO. Besides, graphene itself is 2D structured and thus it will lead to the confined growth of WS_2 in rGO sheets and form the WG nanoslices finally.

As shown in Fig. 2a, the diffraction peaks for the pristine WS_2 index well to the planes of hexagonal WS_2 (JCPDS#84-1398). The clear (002) peak around 14° with an interlayer distance of 0.62 nm indicates the stacked natural of layered WS_2 along the *c* axis. As for the WG composite, the weakened peaks suggest the incorporation of rGO can restrain the stacked natural of WS_2 . The peak around 24° is attributed to rGO sheets.⁶ The (004) peak signal around 29° of WG is relatively weak compared to pristine WS_2 and submerges in background noise, which means the limited crystallinity of layered WS_2 are grown in rGO. There is no other diffraction peak other than WS_2 , indicating the high purity of the

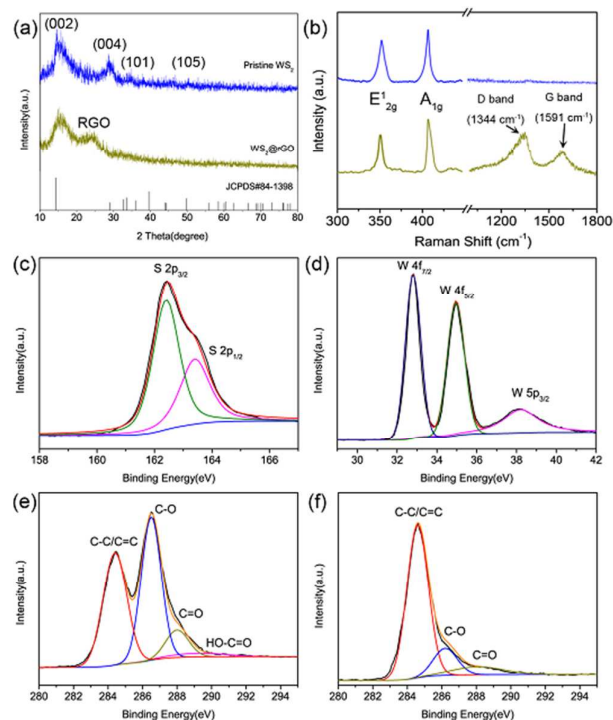


Fig. 2 (a) XRD patterns of the pristine WS₂ and WG composite. (b) Raman spectra of the two structures. (c) S 2p spectrum. (d) W 4f and 5p spectra of WS₂ composite. (e) and (f) are C 1s spectra of GO and WG composite, respectively.

fabricated products. Raman spectroscopy is performed to further confirm the composition of the WG composite. As shown in Fig. 2b, the characteristic Raman shifts at 351 and 415 cm⁻¹ attributed to the in-plane E_{2g}¹ and out-of-plane A_{1g} vibrational modes of hexagonal WS₂, respectively, are clearly observed. The D-band (1344 cm⁻¹) and G-band (1591 cm⁻¹) are related to the defects in graphene shown in Fig. 2b.²⁴ As presented in Fig. 2c, two peaks can be decomposed from 158 eV to 167 eV.²⁵ The peaks at 163.4 and 162.3 eV attribute to the coexistence of S 2p_{1/2} and S 2p_{3/2}. The W 4f_{7/2}, W 4f_{5/2} and W 5p_{3/2} peaks in WS₂ are at binding energies of 32.9, 34.8 and 38.2 eV.²⁶ The high-resolution spectrum of C 1s in Fig. 2e consists of four types of carbon atoms, which shows the presence of C–C/C=C, C–O, C=O and HO–C=O vibrations, exhibiting a large extent of oxidation. As for the C 1s peak-fitting of WG composite shown in Fig. 2f, it only reveals the strong C–C peak and relatively weak peaks of C–O and C=O. The inexistence of the C(O)–O peak suggests the GO sheets have been almost reduced to graphene.

3.2 Electrochemical Performance

Fig. 3a demonstrates the first three cycles of CV for the WG electrode. This CV behaviour is broadly in line with the reported results.¹⁶ For the 1st cathodic sweep, the peak around 0.5 V is ascribed to the formation of Li₂S originated from the conversion reaction (WS₂+4Li→W+2Li₂S). This insertion process of Li ions into WS₂ is accompanied by the decomposition of nonaqueous electrolyte and the degradation of electrolyte along with the formation of solid electrolyte

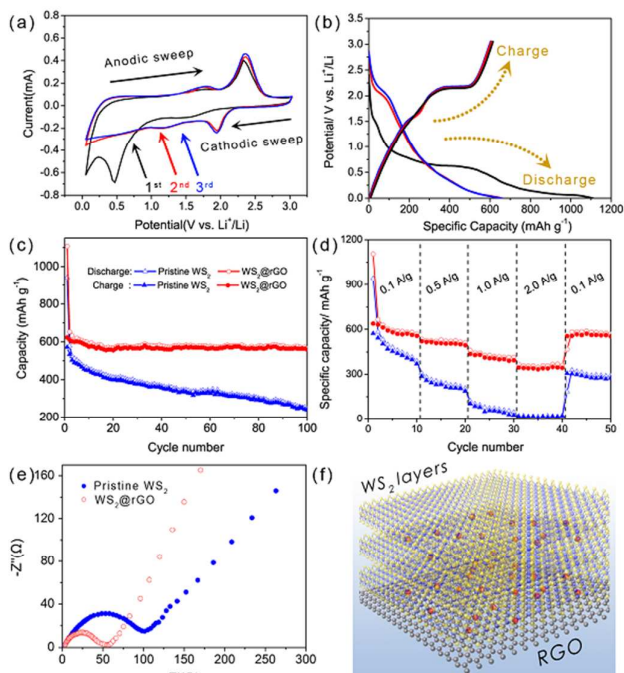


Fig. 3 (a) CV curves of the first three cycles for WG electrode at a scanning rate of 0.5 mV s⁻¹. (b) The first three galvanostatic charge/discharge profiles of WG composite; (c) and (d) Cycling performances and rate capabilities of the two structures. (e) EIS of pristine WS₂ and WG composite electrodes. (f) Schematic diagram of Li ions insertion mode for the WS₂@graphene composite.

interphase (SEI) film. As for the anodic sweeps, the presence of sharp peak at 2.4 V is attributed to the oxidation process of Li₂S into sulfur.²⁷ Therefore, the electrode is mainly composed of W and S instead of WS₂ after the first cycle. Fig. 3b displays the corresponding charge/discharge curves of WG at 0.1 A/g. These profiles confirm the findings from CV. A plateau can be seen around 0.6 V in the first discharge process. This plateau is ascribed to the conversion reaction process in which WS₂ decompose into W particles that embedded in Li₂S and form an octahedral structure. In the following discharge sweeps, the plateau at 0.6 V in the first discharge disappears while a new potential plateau around 2.0 V shows up. As for the charge (delithiation) process, there appears an obvious potential plateau around 2.3 V which is in accord with the above CV curves. In the 1st cycle, the WG electrode delivers a discharge capacity of 1106 mAh/g and the following de-lithiation capacity reaches 602 mAh/g. Generally, the irreversible reactions, such as the formation of SEI film and a portion of Li⁺ trapped in the WS₂ lattice, can lead to the irreversible capacity degeneration in the corresponding lithiation/de-lithiation processes.²⁸ From the second cycle, it is shown that the discharge and charge curves are well overlapped which implies a good cyclical performance has been achieved. The cycle stabilities of the two electrodes at 0.1 A/g are plotted in Fig. 3c. It is obvious that the pristine WS₂ electrode presents a poor capacity retention capability about 200 mAh/g after 100 cycles. It should be noted that the capacity decrease of pristine WS₂/WG composite is sharp while that of the pristine WS₂ is continuous after the first cycle. This can be explained by the

formation of Li_xWS_2 and gel-like polymeric layer resulting from electrochemically driven electrolyte degradation. This is understood as the main reason for sharp decreased capacity in first cycle of the two structures. In the subsequent cycles, accompanying the redox of W nanoparticles and the reversible growth of the gel-like layer should be the plausible reason for the reversible capacity and the sloping voltage regions. Contribution of conversion reaction of Li/WS_2 system on overall capacity was marginally affected by the presence of rGO while Li-irreversibility arising from electrolyte decomposition was greatly suppressed.²⁹ Besides, the fast and obvious capacity degeneration of pristine WS_2 also can be attributed to the low electronic conductivity and the stacked nature of WS_2 . It is remarkable that the cyclic stability of WG composite gets a significant improvement. The WG composite delivers a capacity of about 600 mAh/g in the first few cycles and the capacity can still be retained after 100 cycles. The improved cycling stability can be ascribed to the synergistic effect between WS_2 and rGO nanosheets which can reduce the stacking of WS_2 during lithiation/de-lithiation processes and also facilitate a fast electron and ion transfer. Since the high rate capability is beneficial to the design of LIBs for power-oriented applications, excellent rate performance is also an important aspect.

Fig. 3d shows the superior rate capability of the WG composite compared to the pristine WS_2 . A capacity of ~ 346 mAh/g can still be retained even at the current density of 2 A/g, remaining about half of the initial capacity through 100 cycles with increased charge rate and apparently higher than that of pristine WS_2 . We consider that the stable cycle ability and rate performance of the WG composite are attributed to the following aspects. First, rGO itself is a very good electronic conductor and thus the incorporated rGO can act as the conductive network for the WS_2 sheets to enhance the conductivity of the synthesized composite and promote the charge transfer during discharge/charge processes.⁵ Second, the composite structure can effectively restrain the stacked nature of WS_2 , which will ensure a good electrolyte penetration and utilization of the active substance. The slice-rich morphology of WG composite is readily accessible to the electrolyte and is beneficial to the transfer of Li ions. Besides, the rGO nanosheets with excellent mechanical strength can also restrain the significantly volume change of WS_2 and prevent the degeneration of WS_2 during Li^+ lithiation/de-lithiation processes. In brief, a comprehensive utilization of the advantages of WS_2 and rGO leads to the excellent electrochemical performances for LIBs usage.

An EIS measurement is further performed to investigate the electrochemical performance of WG composite and pristine WS_2 . All measurements in this survey were performed at 60% depth of discharge (DOD) after 10 cycles. The EIS of pristine WS_2 and WG composite are plotted in Fig. 3e. The atomic structure diagram is shown in Fig. 3f. The Nyquist plots of the two electrodes display semicircles in the high frequency region and inclined straight lines in the low frequency region. Generally, the semicircle is associated with the charge-transfer resistance and constant phase element of the

electrode/electrolyte interface, while the inclined line is correlated to the Warburg impedance (Z_w) that reflects the Li ions diffusion.³⁰ The semicircle size of WG electrode is clearly smaller than that of pristine WS_2 , implying the incorporation of rGO can greatly enhance the electrons transfer during electrochemical reactions and lead to a better cycling performance. The composition with rGO can offer a synergistic effect between WS_2 and rGO. The outer electrons of the S atom layer and the π -electrons of the graphene can form an electrons rich cloud and this electrons rich environment can greatly enhance the electrons transfer in the composite structure during lithiation/ de-lithiation processes. It has been reported that the electrons transfer in graphene is 10-fold faster than that in graphite for the presence of corrugation on the graphene surface.³¹ In comparison with the previous reported WS_2 based composite, Bhandavat et al.³² separated bulk WS_2 into few-layer 2-D crystals, the electrochemical behaviour of the WS_2 anode in a lithium half-cell showed a three-step charge-discharge behaviour. The corresponding electrochemical capacity was 118 mAh/g after 50 cycles. Su et al.³³ synthesized WS_2 @graphene nanocomposites via a hydrothermal approach. When applied as anodes in Na-ion batteries, it exhibited about 590 mAh g^{-1} reversible sodium storage capacity and excellent high rate performance.

In summary, 3-dimensional WG nanoslice structured composite has been successfully synthesized through a facile hydrothermal synthesis route. The prepared WG composite exhibited increased capacity, high-rate capability as well as enhanced stability, which can serve as a potential alternative as anode material for LIBs usage.³⁴ The corresponding excellent electrochemical performances of WG composite are mainly attributed to the synergistic effect between WS_2 and rGO. This composite structure can not only prevent the restacking of WS_2 and increase the electric conductivity, but the mechanically robust rGO can buffer volume expansion and alleviate the structure degeneration during lithiation/de-lithiation processes. This facile synthesis approach provides a general route for other rGO-based nanostructures.

3.3 Computational Investigation

In this part, we calculated the charge density difference distribution for WS_2 @graphene composite to further investigate the carriers' migration between WS_2 and graphene. The charge density difference can be expressed as: $\Delta n(\mathbf{r}) = n_{\text{WS}_2@\text{Graphene}}(\mathbf{r}) - n_{\text{WS}_2}(\mathbf{r}) - n_{\text{Graphene}}(\mathbf{r})$, where $n_{\text{WS}_2@\text{Graphene}}(\mathbf{r})$ is the electron density of the WS_2 @Graphene composite, while $n_{\text{WS}_2}(\mathbf{r})$ and $n_{\text{Graphene}}(\mathbf{r})$ are the independent densities of the WS_2 and graphene, respectively.³⁵ The composite structure has been fully relaxed before calculation.

In the calculation of $n_{\text{WS}_2}(\mathbf{r})$ and $n_{\text{Graphene}}(\mathbf{r})$, all atoms in the respective parts are set at the same positions as they were in the composite. This difference can give us the overall information of the charge redistribution. The charge transfer situation between the WS_2 and graphene can be intuitively concluded from these figures. Fig. 4a and b demonstrate the charge density difference of WS_2 @graphene composite. The

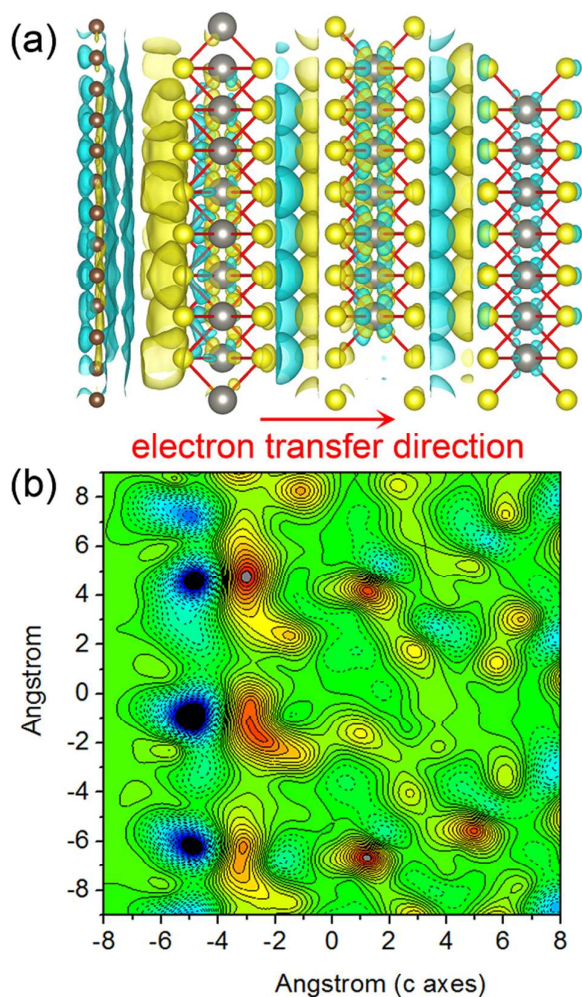


Fig. 4 (a) Charge density difference distribution for WS₂@graphene composite. Depletion and accumulation space are revealed in wathet blue and yellow, respectively. (b) The corresponding density plot in plane passes through basal plane and parallels c axes. The dashed and solid lines denote the regains of charge depletion/accumulation, respectively.

yellow regions in Fig. 4a denote charge accumulation space while the blue indicate the charge depletion. From the difference picture of the WS₂@graphene composite, it means that the charge transfer occurs mainly between graphene layer and the adjacent S atoms layer. The yellow region around S and blue region around graphene layer are clearly larger than other parts, suggesting a certain amount of electrons transfer from graphene to WS₂. Fig. 4b shows (110) surface of the charge density difference, in which red or blue regions represent a gain or loss of charge for the formation of the composite, respectively. According to this contour, it is obvious that there is a charge loss around graphene layer while charge accumulation around the S atoms. Since the electrons can transfer from graphene to WS₂ directionally, the conductivity of the system can be significantly improved and form an electrons rich environment. Next, we calculated the work functions of graphene and WS₂ with respect to the Fermi level and the vacuum level for the two structures. The work

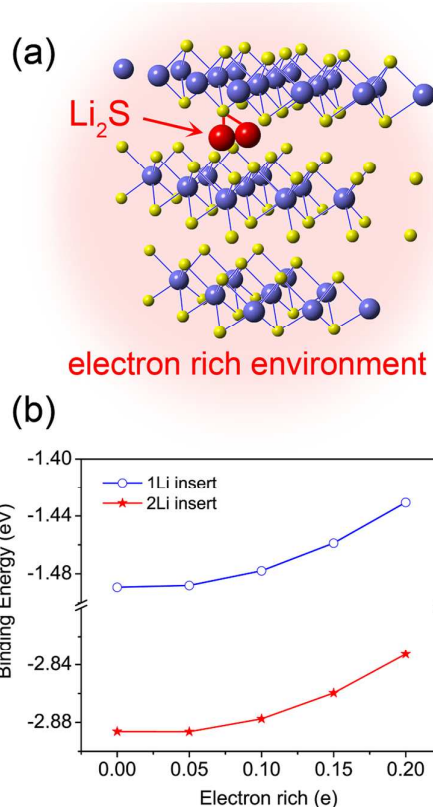


Fig. 5 (a) 2 Li insertion model. (b) The calculated Li binding energies (E^b) for the 1/2-Li inserted structures.

functions of graphene and WS₂ are calculated to be 4.51 and 4.83 eV, respectively. Since the work function position of graphene is higher than that of WS₂, the electrons will flow from graphene to WS₂ directionally when they form a composite structure. Therefore, WS₂ will be positively charged and an electron rich environment was formed for the WS₂. This motivates us to further study what role the electron rich environment is playing for WS₂ in the composite rather than the enhanced conductivity that is known to all.

According to Li *et al.* report,³⁶ the reversible reaction $WS_2 + 4Li \leftrightarrow W + 2Li_2S$ will play a main role in the subsequent processes after the 1st discharge/charge cycle. Thus, we construct the Li₂S mode as shown in Fig. 5a based on this reported structure to conduct the following calculation.³⁷

Binding energy E^b is an important physical quantity to describe the binding characteristic of inserted or adsorbed system. In the following section, we use binding energy to quantitative calculate the insertion of Li to reveal how the directional transfer of electron will influence the corresponding properties. The binding energy of Li is expressed as:³⁸

$$E_{nLi}^b(Ins) = E_{ntot}(Ins) - E_{(n-1)tot}(Ins) - nE_{Li}, n = 1, 2 \quad (1)$$

where $E_{ntot}(Ins)$ is the total energy of n Li inserted structure, $E_{(n-1)tot}(Ins)$ and E_{Li} are the total energy of the $(n-1)$ Li

inserted structure and an independent Li, respectively. The calculated binding energies are plotted in Fig. 5b. The binding energy of 1Li inserted pristine WS₂ in neutral state is -1.489 eV, which is lower than that of 0.2 e rich condition of -1.431 eV. As for the 2Li inserted structure, the corresponding E^b are -2.886 and -2.833 eV, respectively. These calculated results clearly show that the electron rich state has an obvious effect on the binding properties of Li inserted structures. The electrons can directional transfer from graphene network to WS₂ and provide an electron rich environment, this will increase the binding energy of Li insertion. Generally, the improved electrochemical performances of this rGO incorporated composite are commonly attributed to a higher effective interaction area, the restrained formation of SEI film, or the good electrical conductivity for the incorporation of graphene. Herein, we further point out that the higher capacity also has a close relation to the difference of binding energies between pristine and graphene composited WS₂.

According to Eq. 1, it is understandable that a more negative value represents a more energetically stable structure. This may be useful for the purposed insertion or some kinds of performance improvement. With regard to the anode materials used for LIBs, a lower binding energy of lithiation will inevitably lead to a degenerated de-lithiation capacity. It has been concluded that when in the electron rich environment, the interaction between the inserted Li and WS₂ matrix will become weaker as analyzed by the above charge density difference and binding energy analyses. As for the pristine WS₂, the relatively low binding energy will cause considerable amount of Li fixed between the WS₂ interlayers in the form of Li₂S and finally result in a degenerated capacity. However, the synergistic effect between WS₂ and graphene layers will form an electron rich environment when WS₂ composited with graphene, which can effectively increase binding energy and also be beneficial to the following de-lithiation processes. The weakened interaction between Li and WS₂ matrix will facilitate the diffusion of Li through layered WS₂ and restrain the rapid degradation of capacity.

The NEB method is employed to further study the diffusion barriers of Li migration in pristine and graphene composited WS₂ for comparison.³⁹ Between the initial and final constructions for the diffusion routes, each image keeps the equal distance to the neighboring images and searches for the lowest energies along the reaction path.⁴⁰ Linear interpolated 11 images are employed in the corresponding calculation to get the credible barrier energy data.

Generally, the diffusion property mainly depends on the diffusion barrier energy according to the transition state theory.^{41, 42} A lower barrier value will contribute to a faster diffusion rate. As mentioned above that Li₂S will play a leading role in the following electrochemical processes after the 1st discharge/charge cycle, we also construct the Li₂S based configurations for pristine and graphene composited WG as shown in Fig. 6a and conduct the following calculation. Since the geometrical configuration of WG composite is asymmetric, we take three possible paths into account and calculate the

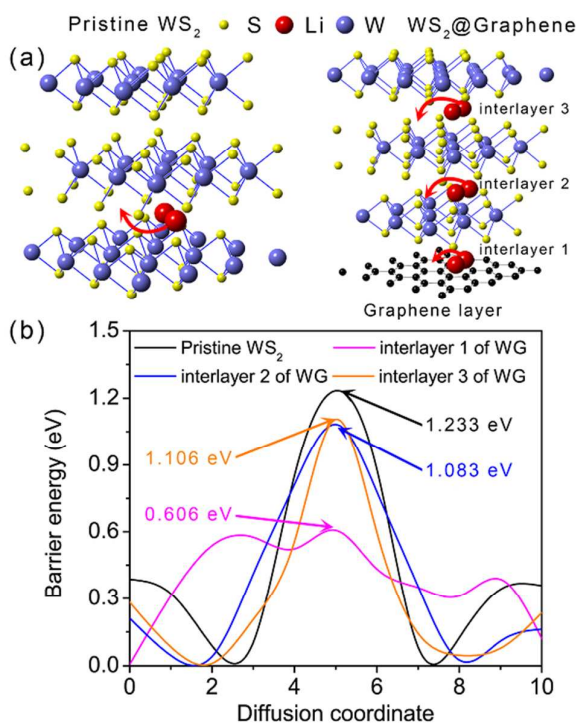


Fig. 6 (a) The schematic diagrams of Li diffusion in pristine and WG composite structure, respectively. As for the WG, three paths of interlayer 1, 2 and 3 are taken into consideration. (b) Diffusion barriers of Li for pristine WS₂ and WG composite structures.

diffusions in interlayers of 1, 2 and 3. The red arrows in Fig. 6a denote the diffusion path of a Li atom from a site of Li₂S to another equivalent site. Fig. 6b shows the computed barrier energies for bulk structured pristine WS₂ and WG composite based on experiment. For the pristine WS₂, the calculated barrier for Li migration is 1.233 eV, while for WG composited structure, the barriers are all decreased. The values for interlayer 1, 2 and 3 are 0.606, 1.083 and 1.106 eV, respectively. Generally, the diffusion coefficient can be expressed as: $D \propto \exp(-E_{\text{barrier}}/k_B T)$, in which k_B and T are the Boltzmann constant and the temperature, respectively. The decrease of energy barriers for the migration of Li in the three interlayers will inevitably induce the increase of diffusivity. Hence, a conclusion is given that the combination with graphene does can increase the migration rate of Li.⁴³ The clearly enhanced diffusivity of Li in the layered WG composite makes it a promising alternative as a desired anode material with a high rate capability. In conclusion, the significantly improved electrochemical performances of WG composite are ascribed to its unique geometrical configuration and electron coupling characteristic. On the one hand, the multi-slices structured WG composite can efficiently shorten the diffusion distance of Li ions, making more efficient use of the active substance. For another, the decreased binding energy of Li insertion will facilitate the de-lithiation process of Li in the electron rich environment based on the first-principles calculation. Besides, the combination with graphene can

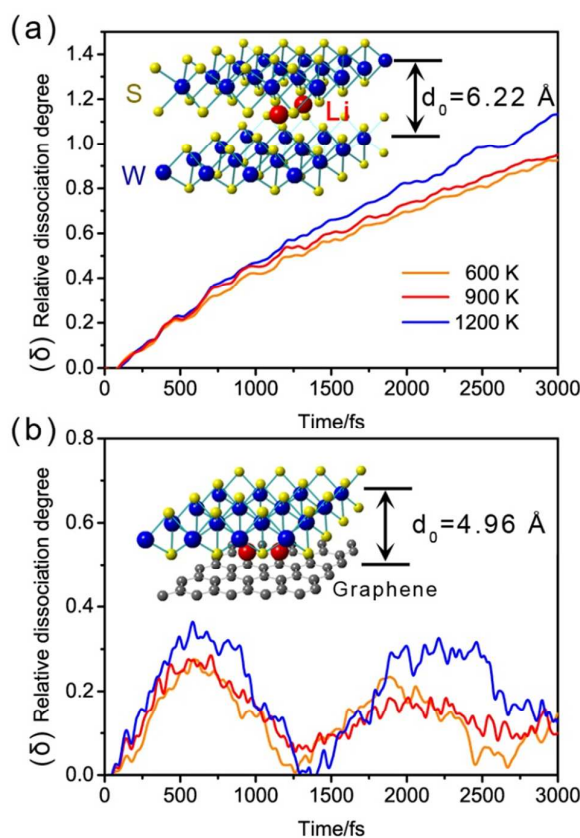


Fig. 7 (a) and (b) are the relative dissociation degree of the pristine and graphene hybrid WS_2 at 600, 900 and 1200 K in 3 ps. Insets are the schematic diagram of 2Li insertion mode for pristine and graphene composited structures, respectively.

effectively lower the barrier energies of Li migration and enhance the diffusivity.

As is well-known that graphene is consisted of sp^2 -bonded aromatic carbon sheets with outstanding properties such as 2D layer structure, excellent electronic conductivity as well as high mechanical strength.⁴⁴⁻⁴⁶ The first two characteristics are intelligible and can be reflected by the measurement methods such as SEM/TEM or EIS. However, the mechanical strength is a rather awkward concept since it is can not be embodied in an intuitionistic way. Herein, we utilize molecular dynamics simulation for the first time to preliminary study the mechanical strength of this WS_2 @graphene structure. First, we define the relative dissociation degree ($\delta = (d - d_0) / d_0$, d denotes the mean distance of basal plane for the adjacent W/C and W atoms, d_0 represents the initial distance) to characterize the stability of the corresponding structures. Starting from the initial configurations at $t=0$ fs and $d=d_0=6.22$ Å as shown in Fig. 7a, atom positions are relaxed at a given temperature for 3000 MD time steps (3 ps). As expected, the values of δ increase linearly with increasing of simulation time for the pristine WS_2 . The unidirectional increased δ and the elevated slope with the increase of temperature indicates a faster dissociation process of the active substance at higher temperatures. As qualitative analyzed above, the poor cycling and rate performances are attributed to the degeneration of the pristine WS_2 structure

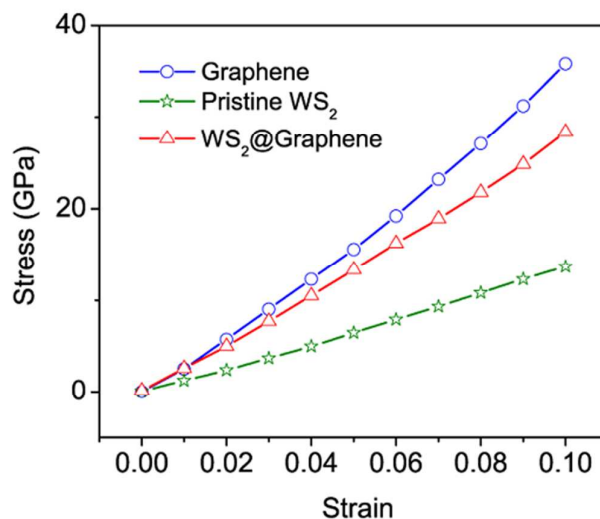


Fig. 8. Stress–strain curve of graphene, pristine WS_2 and WG composite.

during the lithiation/ de-lithiation processes. Hence, it is reasonable to draw a conclusion that when the pristine WS_2 is used as anode material, the degeneration is obvious and irreversible.

When it comes to WS_2 @Graphene composite structure, the variation of δ has a dramatic change. During this time, the integral values of δ for WS_2 @Graphene at three temperatures are all less than 0.4, which has been reached for pristine WS_2 at 1 ps. An another obvious difference between the two structures is that the δ of composite structure has two distinct valley sections, which means this composite structure has some kind of self amendment function, which can effectively suppress the degeneration of active substance during the corresponding lithiation/ de-lithiation processes and this may be because of the excellent mechanical strength of graphene and the synergistic effect between WS_2 /graphene. In brief, we ascribe the excellent electrical conductivity of composite structure to the synergetic effect between WS_2 and rGO. The restrained degeneration of active substance contributes to an improved stability of LIBs, also, the confined growth of multi-slices structured WS_2 on rGO proved by SEM and TEM investigations are free of aggregation. The coupling effect between WS_2 and graphene can accelerate electron transfer and finally facilitate the corresponding electrochemical processes.

To further precisely investigate the cycling stability of the WG composite structure, a stress-strain curve and the corresponding Young's modulus are calculated as shown in Fig. 8. Generally, Young's modulus is a characterization methods to describe the stiffness of an elastic material quantitatively.⁴⁷ It is also known as tensile modulus and related to the bond strength of the material and can be used to describe the mechanical property of the anode materials in this work. Since a specific material can response to the strain with an isotropic in-plane elastic, the Young's modulus can be defined as the ratio of the uniaxial stress over the uniaxial strain which is the slope of the stress–strain curve based on the Hooke's law.

Previously, Andrew et al.⁴⁸ presented an equation of state to characterize how the hydrostatic change in surface area was related to two-dimensional in-plane pressure and yields the measure of a material's resilience to isotropic stretching as one of its fit parameters. Their calculated Young's moduli of graphene was 352.2 GPa based on LDA calculation. It is very similar with our calculated result (357.6 GPa). The Young's modulus of the pristine WS₂ is 138.4 GPa, while the WG composite structure exhibits a much higher value of 258.9 GPa (about 187%) than that of pristine WS₂. This result qualitatively illustrates that the combination with graphene can significantly improve the mechanical property of the WG based anode material and restrain the degeneration of the anode during lithiation-delithiation processes.

4 Conclusion

In summary, WG composite with multi-slices has been successfully synthesized via a simple hydrothermal routine. The morphology and structure of the composite were investigated by SEM, TEM, XRD, Raman spectra and XPS surveys. Electrochemical measurements demonstrated that the WG composite presented a higher capacity, a better rate capability and an enhanced cycle stability compared to that of the pristine WS₂. This composite structure showed a high specific capacity of about 565 mA/g at a current density of 0.1 A/g over 100 cycles. It also could deliver an excellent high rate capacity ~337 mAh/g at a high current density of 2 A/g. The WG composite demonstrated excellent electrochemical performances based on the advantages of conductive rGO network and the effectively suppressed degeneration of WS₂ during lithiation/de-lithiation processes. We further conducted the first-principles calculation analyses. The calculated results revealed that the electrons can directional transfer from graphene network to WS₂ and provide an electron-rich environment, this would increase the binding energy of Li insertion and favor the corresponding de-lithiation process. NEB method was used to investigate the diffusion properties of Li in pristine WS₂ and graphene composite structure. The calculated results indicated that the barrier energies for Li in WS₂@graphene composite were lower than that of in pristine WS₂ and this gave a theoretical account for the better rate performance. Besides, the relative dissociation degree of the composite structure was significantly smaller than that of the pristine WS₂ and could provide an excellent stability. A higher Young's moduli of WG composite in comparison with pristine WS₂ also provided the theoretical explanation for the better cycling performance.

Acknowledgements

The authors acknowledge financial support from the NSF of China (Grant Nos. 61274014, 61474043, 61425004, 61574055), Innovation Research Project of Shanghai Education Commission (Grant No. 13zz033) and Project of Key

Laboratory of Polar Materials and Devices (Grant No. KFKT20140003).

References

- 1 M. H. Chen, X. S. Yin, M. V. Reddy and Stefan Adams, *J. Mater. Chem. A*, 2015, **3**, 10698–10702.
- 2 H. J. Yoo, A. P. Tiwari, J. T. Lee, D. Y. Kim, J. H. Park and H. Lee, *Nanoscale*, 2015, **7**, 3404–3409.
- 3 C. Y. Zhao, J. H. Kong, X. Y. Yao, X. S. Tang, Y. L. Dong, S. L. Phua and X. H. Lu, *ACS Appl. Mater. Interfaces*, 2014, **6**, 6392–6398.
- 4 Y. C. Liu, Y. P. Zhao, L. F. Jiao and J. Chen, *J. Mater. Chem. A*, 2014, **2**, 13109–13115.
- 5 M. Grilic, B. Likozar and J. Levec, *Appl. Catal. B Environ.*, 2014, **150–151**, 275–287.
- 6 K. Chang and W. X. Chen, *Chem. Commun.*, 2011, **47**, 4252–4254.
- 7 H. Hwang, H. Kim and J. Cho, *Nano Lett.*, 2011, **11**, 4826–4830.
- 8 C. S. Reddy, A. Zak and E. Zussman, *J. Mater. Chem.*, 2011, **21**, 16086–16093.
- 9 Q. Wang and J. Li, *J. Phys. Chem. C*, 2007, **111**, 1675–1682.
- 10 Y. G. Guo, X. Zhou and L. J. Wan, *Chem. Commun.*, 2013, **49**, 1838–1840.
- 11 J. Z. Wang, L. Lu, M. Lotya, J. N. Coleman, S. L. Chou, H. K. Liu, A. I. Minett and J. Chen, *Adv. Energy Mater.*, 2013, **3**, 798–805.
- 12 P. Y. Gao, Z. X. Yang, G. M. Liu and Q. D. Qiao, *Ceram. Int.*, 2015, **41**, 1921–1925.
- 13 L. C. Yang, S. N. Wang, J. J. Mao, J. W. Deng, Q. S. Gao, Y. Tang and O. G. Schmidt, *Adv. Mater.*, 2012, **25**, 1180–1184.
- 14 K. Chang, D. S. Geng, X. F. Li, J. L. Yang, Y. J. Tang, M. Cai, R. Y. Li and X. L. Sun, *Adv. Energy Mater.*, 2013, **3**, 839–844.
- 15 G. D. Li, X. Y. Zeng, T. D. Zhang, W. Y. Ma, W. P. Lia and M. Wang, *CrystEngComm*, 2014, **16**, 10754–10759.
- 16 K. Shiva, H. S. S. Ramakrishna Matte, H. B. Rajendra, A. J. Bhattacharyya and C. N. R. Rao, *Nano Energy*, 2013, **2**, 787–793.
- 17 K. N. Dip, K. S. Uttam, C. Devika, M. Sagar and K. S. Shaibal, *Electrochimica Acta*, 2014, **146**, 706–713.
- 18 Y. Liu, W. Wang, Y. W. Wang and X. S. Peng, *Nano Energy*, 2014, **7**, 25–32.
- 19 X. D. Xu, C. S. Rout, J. Yang, R. G. Cao, P. Oh, H. S. Shin and J. Cho, *J. Mater. Chem. A*, 2013, **1**, 14548–14554.
- 20 Y. T. Liu, X. D. Zhu, Z. Q. Duan and X. M. Xie, *Chem. Commun.*, 2013, **49**, 10305–10307.
- 21 Y. Liu, W. Wang, L. Gu, Y. W. Wang, Y. L. Ying, Y. Y. Mao, L. W. Sun, X. S. Peng, *ACS Appl. Mater. Interfaces*, 2013, **5**, 9850–9855.
- 22 T. Liang, S. W. Gregory, S. P. Scott, B. S. Susan and R. P. Simon, *J. Phys. Chem. C*, 2011, **115**, 10606–10616.
- 23 M. Kan, J. Y. Wang, X. W. Li, S. H. Zhang, Y. W. Li, Y. Kawazoe, Q. Sun and P. Jena, *J. Phys. Chem. C*, 2014, **118**, 1515–1522.
- 24 R. H. Wang, C. H. Xu, J. Sun, L. Gao and C. C. Lin, *J. Mater. Chem. A*, 2013, **1**, 1794–1800.
- 25 H. T. Wang, Z. Y. Lu, D. S. Kong, J. Sun, T. M. Hymel and Y. Cui, *ACS Nano*, 2014, **5**, 4940–4947.
- 26 S. S. Xu, X. M. Gao, M. Hu, J. Y. Sun, D. S. Wang, F. Zhou, L. J. Weng and W. M. Liu, *Surf. Coat. Tech.*, 2014, **238**, 197–206.
- 27 V. H. Pham, K. H. Kim, D. W. Jung, K. Singh, E. S. Oh and J. S. Chung, *J. Power Sources*, 2013, **224**, 280–286.
- 28 J. Xiao, X. J. Wang, X. Q. Yang, S. D. Xun, G. Liu, P. K. Koech, J. Liu and J. P. Lemmon, *Adv. Funct. Mater.*, 2011, **21**, 2840–2846.
- 29 L. David, R. Bhandavat, U. Barrera and G. Singh, *Sci. Rep.*, 2015, **5**, 9792.

- 30 S. Hu, W. Chen, J. Zhou, F. Yin, E. Uchaker, Q. F. Zhang and G. Z. Cao, *J. Mater. Chem. A*, 2014, **2**, 7862–7872.
- 31 W. Li, C. Tan, M. A. Lowe, H. D. Abruna and D. C. Ralph, *ACS Nano*, 2011, **5**, 2264–2270.
- 32 R. Bhandavat, L. David, and G. Singh, *J. Phys. Chem. Lett.*, 2012, **3**, 1523–1530.
- 33 D. W. Su, S. X. Dou and G. X. Wang, *Chem. Commun.*, 2014, **50**, 4192–4195.
- 34 Z. Wang, T. Chen, W. X. Chen, K. Chang, L. Ma, G. C. Huang, D. Y. Chen and J. Y. Lee, *J. Mater. Chem. A*, 2013, **1**, 2202–2210.
- 35 B. Chilukuri, U. Mazur and K. W. Hipps, *Phys. Chem. Chem. Phys.*, 2014, **16**, 14096–14107.
- 36 Y. Li, W. Wang, H. B. Huang, L. Gu, Y. W. Wang and X. S. Peng, *Chem. Commun.*, 2014, **50**, 4485–4488.
- 37 S. Tyler, Z. Li, O. Brian and M. David, *Energy Environ. Sci.*, 2014, **7**, 209–231.
- 38 C. G. Van de Wallea and J. Neugebauer, *J. Appl. Phys.*, 2004, **95**, 3865–3870.
- 39 G. Henkelman, B. P. Uberuaga and H. Jonsson, *J. Chem. Phys.*, 2000, **113**, 9901–9904.
- 40 R. A. Olsen, G. J. Kroes and G. Henkelman, *J. Chem. Phys.*, 2004, **121**, 9776–9792.
- 41 B. Kang and G. Ceder, *Nature*, 2009, **458**, 190–193.
- 42 G. H. Vineyard, *J. Phys. Chem. Solids*, 1957, **3**, 121–127.
- 43 J. C. Su, Y. Pei, Z. H. Yang and X. Y. Wang, *Comp. Mater. Sci.*, 2015, **98**, 304–310.
- 44 Z. S. Wu, W. C. Ren, L. Wen, L. B. Gao, J. P. Zhao, Z. P. Chen, G. M. Zhou, F. Li and H. M. Cheng, *ACS Nano*, 2010, **4**, 3187–3194.
- 45 R. Muszynski, B. Seger and P. V. Kamat, *J. Phys. Chem. C*, 2008, **112**, 5263–5266.
- 46 X. Huang, Z. Y. Zeng, Z. X. Fan, J. Q. Liu and H. Zhang, *Adv. Mater.*, 2012, **24**, 5979–6004.
- 47 D. L. Miao, J. B. Wu, J. J. Jiang and P. Liang, *J. Phys. Chem. C*, 2013, **117**, 23–27.
- 48 R. C. Andrew, R. E. Mapasha, A. M. Ukpogon and N. Chetty, *Phy. Rev. B*, 2012, **85**, 125428.